Nanoscale Advances

ROYAL SOCIETY OF CHEMISTRY

PAPER

View Article Online
View Journal | View Issue

Check for updates

Cite this: *Nanoscale Adv.*, 2026, **8**, 2675

Multifunctional PAA- and PEG-modified $Co_3V_2O_8$ nanoparticles for enhanced RhB degradation, OER activity, and antibacterial activity: experimental validation and computational insight

Arbab Munir,[a] Muhammad Imran,[b] Iram Shahzadi,[c] Ali Haider,[d] Zernab Mateen,[e] Anwar Ul-Hamid,[f] Norah A. Albassami[g] and Muhammad Ikram *[e]

Developing earth-abundant, cost-effective, sustainable and efficient multifunctional catalysts for the oxygen evolution reaction (OER), catalytic dye degradation, and antibacterial activity is extremely challenging. Herein, a novel ternary heterogeneous catalyst, polyacrylic acid/polyethylene glycol-cobalt vanadate nanoparticles (PAA/PEG-$Co_3V_2O_8$ NPs), was synthesized using a co-precipitation method. This study reported the multifunctionality of PAA/PEG-$Co_3V_2O_8$ in degrading RhB, enhancing OER activity, and inhibiting multiple drug-resistant *Staphylococcus aureus* (MDR *S. aureus*), with molecular docking analysis providing insights into binding interactions. The samples were comprehensively analyzed using an array of analytical techniques, including XRD, SAED, FTIR spectroscopy, UV-Vis spectroscopy, TEM, HRTEM, and EDS. The electrochemical activity of the prepared material was evaluated by linear sweep voltammetry (LSV) and electrochemical impedance spectroscopy (EIS). The optimized sample exhibited a maximum degradation of 96.34% in an acidic medium within 10 minutes and demonstrated minimal overpotentials of 270, 299, and 362 mV at 30, 50, and 100 mA cm^{-2}, respectively. The lowest Tafel slope and charge-transfer resistance indicated the superior OER performance. The optimized material showed a maximum inhibition zone of 8.25 ± 0.93 mm against MDR *S. aureus*. The bactericidal action of PAA/PEG-$Co_3V_2O_8$ NPs was further elucidated through molecular docking, which substantiated their role in the inhibition of topoisomerase II DNA gyrase and dihydrofolate reductase (DHFR) in *S. aureus*. These findings demonstrate the role of PAA and PEG in improving the overall activity of $Co_3V_2O_8$, yielding a pathway for fabricating an efficient, cost-effective, and sustainable material for environmental remediation and water-splitting applications.

Received 11th December 2025
Accepted 15th March 2026

DOI: 10.1039/d5na01130b

rsc.li/nanoscale-advances

Open Access Article. Published on 16 March 2026. Downloaded on 6/5/2026 2:20:00 AM. This article is licensed under a Creative Commons Attribution-NonCommercial 3.0 Unported Licence.

1. Introduction

Water is essential for sustaining life.[1] Industrialization has increased the release of toxic heavy metals, posing threats to living species. Several industrial sectors (textile, chemical processing, plastic, and paper) release a large number of cationic and anionic dyes, such as methylene blue, rhodamine B (RhB), methyl orange, and Procion Red, into water bodies.[2–4] RhB, a fluorescent tracer in textiles and foods, is carcinogenic and causes reproductive, neurological, and chronic toxicity. Their direct discharge into water causes skin, eye, and respiratory tract irritations.[5,6] Multiple wastewater treatment methods have been reported in the literature, such as ozonation, ion exchange, adsorption, coagulation–flocculation, electrochemical, and biological treatments. However, these methods have some limitations, including high chemical consumption, operational costs, and sludge production. Catalysis is an economical and energy-efficient method for wastewater treatment.[7] Rapid population expansion and industrialization have significantly increased energy consumption.[8] Clean energy sources, such as solar, tidal, wind and hydrogen, have been introduced. Among them, hydrogen with a high energy density of 140 MJ kg^{-1} is considered an efficient energy source.[9] Electrochemical water splitting (EWS) has garnered significant

[a]*Department of Physics, Government College University, Faisalabad, Pakpattan Road, Sahiwal, Punjab, 57000, Pakistan*

[b]*Interdisciplinary Research Center for Hydrogen Technologies and Carbon Management (IRC-HTCM), King Fahd University of Petroleum & Minerals, Dhahran 31261, Saudi Arabia*

[c]*School of Pharmacy, University of Management and Technology, Lahore, 54770, Pakistan*

[d]*Department of Clinical Sciences, Faculty of Veterinary and Animal Sciences, Muhammad Nawaz Shareef, University of Agriculture, Multan 66000, Punjab, Pakistan*

[e]*Solar Cell Applications Research Lab, Department of Physics, Government College University Lahore, Lahore 54000, Punjab, Pakistan. E-mail: dr.muhammadikram@gcu.edu.pk*

[f]*Core Research Facilities, King Fahd University of Petroleum & Minerals, Dhahran 31261, Saudi Arabia*

[g]*Chemistry Department, Faculty of Science, King Khalid University, P. O. Box 9004, Abha, 61413, Saudi Arabia*

© 2026 The Author(s). Published by the Royal Society of Chemistry

Open Access Article. Published on 16 March 2026. Downloaded on 6/5/2026 2:20:00 AM. This article is licensed under a Creative Commons Attribution-NonCommercial 3.0 Unported Licence.

interest for capturing hydrogen and storing energy *via* the OER and HER in the form of chemical energy. O_2 production at the anode and H_2 at the cathode *via* EWS is one of the promising cost-effective and environmentally benign approaches for sustainable energy conversion.[10,11] Despite its advantages, water splitting requires a large overpotential apart from the thermodynamic potential (1.23 V) due to the sluggish OER kinetics, particularly due to the complex multi-electron process. Noble OER electrocatalysts (RuO_2 and IrO_2) demonstrate high OER activity, but their high cost limits their application.[12] Therefore, there is an urgent need for developing low cost, robust electrocatalysts that function at minimal overpotentials and improve the kinetics and efficiency of the reaction.[13] Additionally, among various diseases (hepatitis, mastitis, typhoid, and diarrhea) caused by microorganisms, mastitis is a prevalent issue in dairy production systems nationwide, resulting in significant economic losses. It is a commonly reported disease and is linked to production-related factors in dairy farms. Mastitis is associated with physicochemical or traumatic variation in milk and pathological changes in mammary glands.[14–16] *S. aureus* is one of the most contagious pathogens associated with mastitis etiology.[15]

Transition metal oxides, hydroxides, chalcogenides, and their composites are widely used as catalysts for electrocatalytic OER. Materials having Co and V stand out as effective catalysts, attributed to the presence of V that promotes fast charge-transfer and facilitates the OER activity.[17] Several vanadates, including $BiVO_4$, $SmVO_4$, Ag_3VO_4, and $Co_3V_2O_8$, were used for dye degradation, OER, and antimicrobial activity. $Co_3V_2O_8$ has great potential in multiple fields, including supercapacitors,[18] electrodes for lithium-ion batteries,[19] and catalysis.[20] $Co_3V_2O_8$ has emerged as a potential candidate for pollutant degradation and as a robust catalyst for OER, ascribed to the synergistic effect of different metal ions.[8,21–25] A previous study reported that multilayered $Co_3V_2O_8$ nanosheets exhibit better activity than single-phase oxides, ascribed to the combined effect between metals in mixed metal oxides that improves stability and electrical conductivity.[19] Ding *et al.* reported that $Co_3V_2O_8$ demonstrates improved photocatalytic and electrocatalytic activity relative to cobalt oxides.[20] Metal ions (silver, copper, cobalt, vanadium, and zinc) are considered as efficient antibacterial agents. As reported in previous studies, vanadium compounds (V_2O_3, VO_2, and V_2O_5), particularly V_2O_5, show enhanced bactericidal activity because of their high valence states. $Co_3V_2O_8$ shows significant antibacterial potential attributed to the generation of reactive oxygen species (ROS) that damages bacterial cells and induces oxidative stress[26]. The co-precipitation method is a simple, efficient, and cost-effective technique for NMs synthesis.[27] The catalytic, electrochemical, and antibacterial activities of $Co_2V_3O_8$ were enhanced with polyethylene glycol (PEG) and polyacrylic acid (PAA). PEG, as a capping agent, is widely used for boosting catalytic and antibacterial properties, owing to its solubility, low toxicity, biocompatibility, and thermal stability.[28] Its organized chain-like structure makes it widely used as a capping agent in nanoscale material synthesis. PEG functions as a growth template in NMs synthesis and improves the structural, surface, and crystallographic properties of the material. Several studies have reported that PEG improves the antibacterial and degradation activity of materials.[28–30] PEG modifies the electronic structure and improves charge transport at the electrode interface and charge storage efficiency.[31] Further, PAA is a polymer of acrylic acid monomers and is highly effective in eliminating pollutants because of its carboxyl groups (COOH) that enable the efficient adsorption of heavy metal ions and dyes from wastewater.[32,33] The ability of PAA to make metal complexes is ascribed to the large number of COOH, coupled with hydrophilicity and mechanical stability, which enables it to increase the electrochemical activity of the material.[34] One study investigated the influence of PAA concentration on the electrochemical activity of the material. Findings reveal that optimized Mo–Ni oxides tailored with PAA show an OER overpotential of 330 mV to achieve a current density of 10 mA cm^{-2}.[35] It also improves the antibacterial properties against Gram-positive and Gram-negative bacterial and fungal strains.[36]

In this study, a simple and environmentally benign co-precipitation route was employed to synthesize the PAA/PEG-modified $Co_2V_3O_8$ NPs. The structural, functional, optical, and morphological characteristics of the synthesized NPs were examined using XRD, FTIR, UV-Vis spectrophotometer, TEM, and HRTEM. The novel PAA/PEG-$Co_2V_3O_8$ NPs were assessed for their catalytic ability to degrade RhB, OER activity, and antimicrobial effectiveness against *S. aureus*.

2. Material section

2.1 Material

Ammonium metavanadate (NH_4VO_3 >99%), polyacrylic acid, polyethylene glycol, NaOH (>98%), HCl (37%), ethanol (C_2H_5OH ≥99.8%), Nafion, RuO_2, and sodium borohydride ($NaBH_4$) were acquired from Sigma-Aldrich (Germany). Cobalt(II) nitrate hexahydrate ($Co(NO_3)_2 \cdot 6H_2O$) was procured from VWR Chemicals, and polyethylene glycol was attained from Fluka Chemicals. KOH was purchased from MERCK.

2.2 Synthesis of $Co_3V_2O_8$, PEG-$Co_3V_2O_8$, (2 wt% and 4 wt%) PAA/PEG-$Co_3V_2O_8$

The co-precipitation route was employed to synthesize $Co_3V_2O_8$ and 3 wt% PEG and different concentrations (2 and 4 wt%) of PAA-doped $Co_3V_2O_8$. Initially, 0.4 M of $Co(NO_3)_2$ and NH_4VO_3 were dissolved in deionized (DI) water (100 mL). The solution was continuously stirred and heated at 90 °C for 45 minutes to ensure homogeneity. An appropriate concentration of the precipitating agent (NaOH) was integrated to attain a pH of ~11, facilitating the formation of precipitates. To synthesize PAA and PEG doped $Co_3V_2O_8$, the predetermined amounts of PEG and PAA were incorporated into the prepared solutions of $Co(NO_3)_2$ and NH_4VO_3 prior to adjusting the pH. The acquired precipitates were centrifuged at 8000 rpm for 8 minutes, and subsequently rinsed thoroughly with DI water to eliminate the impurities. The washed residues were heated at 150 °C for 12 h and crushed to get fine powders (Fig. 1).

© 2026 The Author(s). Published by the Royal Society of Chemistry

Open Access Article. Published on 16 March 2026. Downloaded on 6/5/2026 2:20:00 AM. This article is licensed under a Creative Commons Attribution-NonCommercial 3.0 Unported Licence.

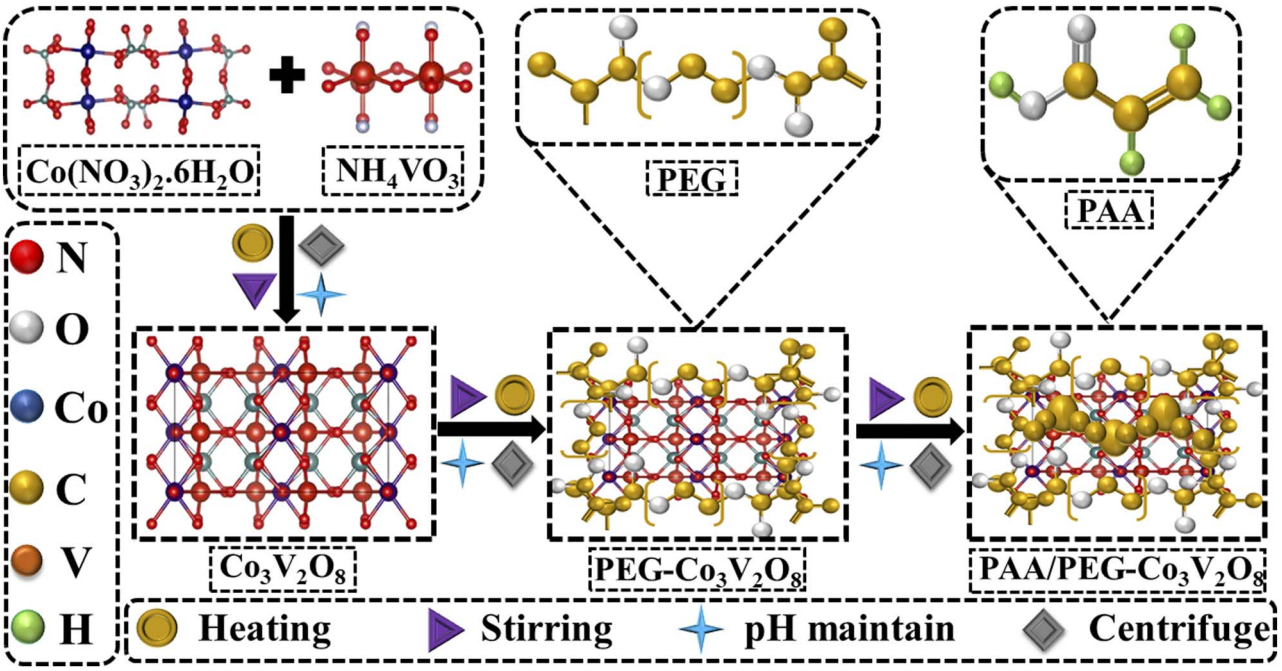

Fig. 1 Schematic synthesis diagram of PAA/PEG-$Co_3V_2O_8$.

2.3 Catalytic activity (CA)

The degradation efficiency of undoped and doped $Co_3V_2O_8$ nanocatalysts (NCs) in the presence of $NaBH_4$ were assessed by monitoring the UV-Vis spectra at specified time intervals. Firstly, 400 μL (NCs and $NaBH_4$) were added to 3 mL RhB in a quartz cell. The degradation of the dye was evaluated by monitoring the absorption spectra at predetermined intervals with a UV-Vis spectrophotometer operating at room temperature. The NCs accelerated the RhB degradation by a reduction reaction facilitated by $NaBH_4$, resulting in the transformation of RhB into leuco RhB (LRhB). The degradation efficiency was computed using the equation below (eqn (1)):

$$\text{Degradation (\%)} = (C_0 - C_t)/C_0 \times 100 \quad (1)$$

where C_0 and C_t show the initial and final RhB concentrations.

2.4 Electrode preparation

Ni foam (NF) measuring (1 × 2 cm^2) was used as a substrate for the deposition of the electrocatalyst. NF was activated by sonification in dilute HCL, followed by sequential sonification in ethanol and DI water for 30 minutes each. The cleaned NF was then dried under an IR lamp. The working electrode was prepared by forming a homogeneous mixture of 5 mg of the prepared sample ($Co_3V_2O_8$ and doped $Co_3V_2O_8$), ethanol (600 μL), and Nafion (20 μL). The mixture was sonicated for 30 minutes to attain a homogeneous electrocatalyst slurry. The resultant slurry was uniformly drop-cast onto a pretreated NF substrate of area 1 × 1 cm^2 using a micropipette, ensuring uniform coating and penetration onto the substrate. The electrocatalyst-deposited NF was then dried under an IR lamp.

2.5 Electrochemical analysis

Electrochemical measurements of the prepared electrocatalyst were performed on the Corrtest CS350M electrochemical workstation at ambient temperature. To conduct this study, three electrode configurations, comprising an Ag/AgCl electrode (reference electrode), a platinum plate with dimensions 1 × 1 × 0.1 mm (counter electrode), and an electrocatalyst-deposited Ni foam (working electrode), were employed. Overpotential of Ni foam was 308 mV at 10 mA cm^{-2} from our previous study (https://doi.org/10.1002/adsu.202500317). All measurements were carried out in an alkaline medium (1 M KOH). The electrocatalytic performance was assessed by performing LSV at a scan rate of 5 mV s^{-1} within the optimized potential window to measure the overpotentials at the desired current density relative to reference (Ag/AgCl) at a positive applied potential. The reverse LSV scan was used to ensure that no NF oxidation peak overlaps with the catalyst intrinsic response.[37] The measured potentials were converted into RHE (reversible hydrogen electrode) using the following equation (eqn (2))

$$E_{RHE} = E_{Ag/AgCl} + 0.059 \times pH + E^0_{Ag/AgCl} \quad (2)$$

where $E_{Ag/AgCl}$ denotes the potential *vs.* Ag/AgCl.

$E^0_{Ag/AgCl}$ is the standard redox potential of Ag/AgCl at 25 °C.

The overpotentials (η) were computed using equation (eqn (3)).

$$\eta\ (V) = E_{RHE} - 1.23\ V \quad (3)$$

The reaction kinetics and efficiency of the electrocatalyst were evaluated using the Tafel slope acquired from the linear fitting of the Tafel plot. For this evaluation, the following relation (eqn (4)) was employed.

Open Access Article. Published on 16 March 2026. Downloaded on 6/5/2026 2:20:00 AM. This article is licensed under a Creative Commons Attribution-NonCommercial 3.0 Unported Licence.

$$\eta = \alpha + b \log j \quad (4)$$

where η denotes the overpotential, b is the Tafel slope, and a is constant.

Subsequently, the EIS was performed over the frequency range of 0.01–100 kHz within an applied AC perturbation of 10 mV to measure the resistive parameters.

2.6 Isolation and identification of MDR *S. aureus*

2.6.1 Sample acquisition. Raw milk samples, clinically positive for bovine mastitis, were acquired from various locations (dairy farms, veterinary clinics) in Punjab, Pakistan. The samples were promptly transferred in sterilized containers and kept at 4 °C while being transported to the laboratory. To identify the presence of *S. aureus*, the specimens were inoculated on mannitol salt agar, following incubation at 37 °C for two days.

2.6.1.1 Identification and characterization of bacteria isolates. The initial identification of *S. aureus* was carried out by analyzing colony morphology, followed by Gram's staining and series of biochemical assays, adhering to the mentioned procedures in Bergey's Manual of Determinative Bacteriology.[38]

2.6.1.2 Antibiotic susceptibility. The antibiotic susceptibility was assessed using the disk diffusion method by Bauer *et al.* on Mueller Hinton agar (MHA) to evaluate antibiotic resistance.[39] The test evaluated the *S. aureus* resistance against various classes of antibiotics, including gentamicin (10 μg), imipenem (10 μg), azithromycin (15 μg), tetracycline (30 μg), amoxicillin (30 μg), and ciprofloxacin (CIP) (5 μg), representing aminoglycosides, carbapenems, macrolides, tetracyclines, penicillins, and quinolones.[40] *S. aureus* was standardized to a turbidity of 0.5 MacFarland and then cultured on MHA plates. To prevent the overlapping inhibition zones, the antibiotic discs were arranged accordingly, and the cultured plates were incubated for 24 h at 37 °C. The findings were analyzed according to the standard guidelines by the CLSI.[41] The bacterium was identified as a multiple drug-resistant (MDR) microorganism if found resistant to at least three different antibiotic classes.[42]

2.6.1.3 Antimicrobial activity. The bactericidal effectiveness of the prepared specimens was evaluated against MDR *S. aureus via* the agar well diffusion method. This assessment was performed on ten segregates acquired from mastitic milk. Mannitol salt agar plates were swabbed with a 0.5 McFarland standard growth of MDR *S. aureus*. Six-millimeter wells were formed *via* a sterile cork borer. 0.005 mg/50 μL of CIP and 50 μL of DI water were used as the positive and negative references, respectively. The antimicrobial activity of the zero-doped and doped NPs was assessed at concentrations of 0.5 and 1.0 mg/50 μL. After incubation, the inhibition zone diameters were measured *via* a digital vernier caliper.[43,44]

2.6.1.4 Statistical analysis. Statistical analysis was conducted using SPSS 24.0, employing one-way analysis of variance (ANOVA) upon diameters of calibrated inhibition zones (mm).[15]

2.7 Molecular docking analysis

Docking analysis was performed relying on the SYBYL-X 2.0 program to comprehend the suppressive mechanism and interactions involving PAA/PEG-$Co_3V_2O_8$.[45] In order to preemptively address the inhibition of protein synthesis, this approach involved targeting and obstructing DNA gyrase (topoisomerase II) and folate synthesis, a crucial enzyme integral to the DNA replication mechanism. The protein data bank provided the three-dimensional structures of the gyrase complex with DNA and ciprofloxacin, as well as DHFR, accessed *via* the 2XCT[46] and 3FYW codes.[47] The model complex of PAA/PEG-$Co_3V_2O_8$ was constructed utilizing the Sybyl-X2.0/SKETCH module. Subsequently, the Tripos force field and Gasteiger Hückel atomic charge were utilized to ensure energy conservation. A convergence gradient of 0.05 kcal $(mol)^{-1}$ was achieved, following 1000 cycles of energy reduction through the Powell technique. The Surflex-Dock module that incorporates Hammerhead's empirical scoring mechanism, involving a molecular similarity approach (morphological similarity), alongside D-score (dock score), G-score (gold score), Chem-Score, potential mean force (PMF) score, and/or complete score, facilitated the execution of versatile molecular docking simulations.

3. Results and discussion

XRD analysis was carried out to ascertain the crystallographic structure, plane orientation, and phase composition of the prepared NPs. The XRD spectra were analyzed within the $2\theta°$ range of (18–70°), as shown in Fig. 2a. The diffraction peaks at 18.75°, 31.08°, 35.28°, 42.98°, 61.93°, and 62.69° were assigned to the crystallographic planes (021), (040), (221), (133), (333), and (172), corroborating the orthorhombic phase of $Co_3V_2O_8$, along with the space group of *Cmca* synchronized with JCPDS card no. 96-100-7076. The peak at 30.0° (220) was related to the cubic structure of $Co_3V_2O_8$.[48] An additional peak flexing at 29.3°, corresponding to the $(\bar{1}11)$ plane, revealed the monoclinic configuration of CoV_2O_6, along with space group *C*2, well indexed with JCPDS card no. 01-077-1174. With the addition of PEG, a new peak emerged at 19.27°, indicating the successful incorporation of PEG into the sample.[49] The PEG and PAA addition decreased the peak intensity and broadening, attributed to the capping effect and its amorphous nature.[28] The SAED analysis indicates the polycrystalline nature of $Co_3V_2O_8$ and 4 wt% PAA/PEG-$Co_3V_2O_8$ with discrete bright circular rings. These discrete rings were well indexed with the different crystallographic facets of the XRD pattern, as illustrated in Fig. 2b and c.

The presence of functional groups, chemical skeleton, and vibrational modes in the synthesized NPs was scrutinized by analyzing the FTIR spectra within the wavenumber range (4000–450 cm^{-1}), as shown in Fig. 3a. The broad transmittance band centered at 3000–3600 cm^{-1} indicates the stretching vibration of the –OH group, indicative of hydrogen bonding.[25] A weak band at ~2337 cm^{-1} is associated with the symmetric stretching vibration of H–O–H adsorbed on the material surface, while the prominent band at 2122 cm^{-1} indicates the existence of free water characterized by O–H vibrations.[50,51] The sharp band at 1644 cm^{-1} is characteristic of the C═N stretching vibration.[25] The prominent band at ~1396 cm^{-1} arises from nitrate residues from the reactant.[51] The manifested band at ~933 cm^{-1} is

 © 2026 The Author(s). Published by the Royal Society of Chemistry

Open Access Article. Published on 16 March 2026. Downloaded on 6/5/2026 2:20:00 AM.
This article is licensed under a Creative Commons Attribution-NonCommercial 3.0 Unported Licence.

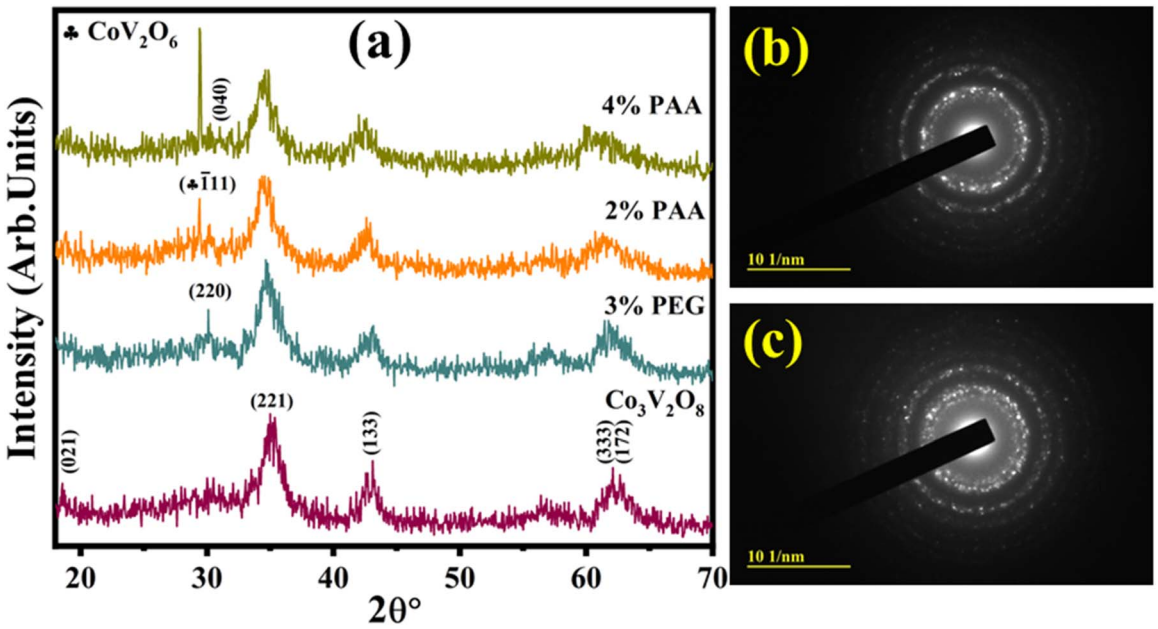

Fig. 2 (a) XRD spectra of the synthesized NPs and (b and c) SAED images of $Co_3V_2O_8$ and 4 wt% of the PAA-doped PEG-$Co_3V_2O_8$ NPs.

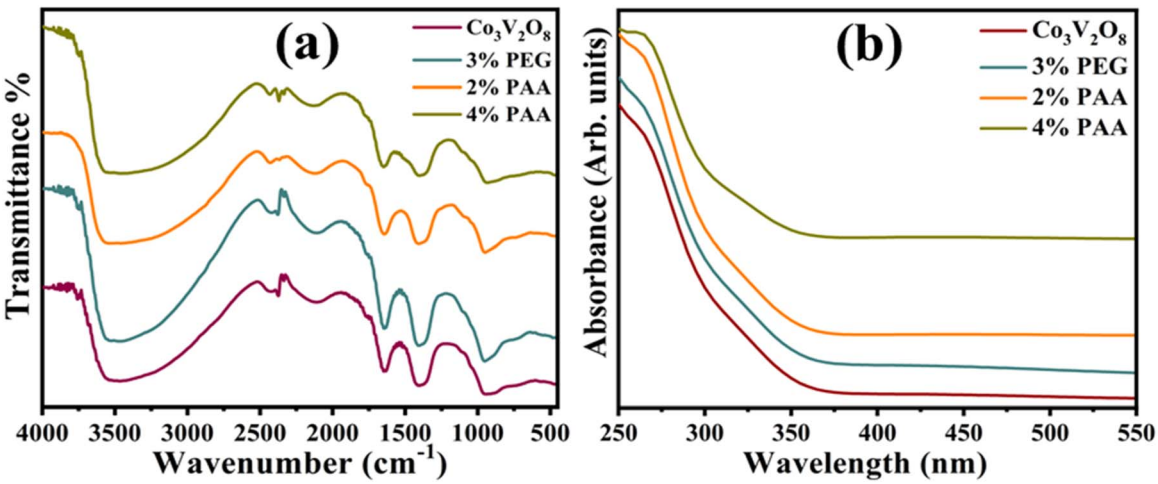

Fig. 3 (a) FTIR spectra and (b) absorption spectra of $Co_3V_2O_8$, PEG-$Co_3V_2O_8$, (2 and 4 wt%) PAA/PEG-$Co_3V_2O_8$ NPs.

ascribed to the V=O symmetrical stretching mode.[51] The vibrational modes associated with Co–O and V–O–V bonds were validated by the band at 561 cm^{-1}.[52] The band observed at 467 cm^{-1} is attributed to the vibrational modes associated with the extended Co–O, Co–O–Co, and Co–O–V linkages.[53] Upon PEG incorporation, an increase in the band intensities was observed, confirming the interaction and complexation between PEG and $Co_3V_2O_8$.[54,55] The transmittance bands within the 2300–2500 cm^{-1} range initially merge with the addition of PAA. In contrast, these bands reappear as the additive amount of PAA increases. Electronic spectroscopy was conducted to investigate the optical properties of the doped and undoped NPs. The obtained spectra were examined to determine the maximum absorption wavelength (λ_{max}) and band gap energies (E_g) within the 250–550 nm wavelength range (Fig. 3b). The maximum absorption observed at 266 and 325 nm was linked with the Co–V bond, indicating charge transfer between Co, V and oxygen atoms. This absorption shoulder verified the metal–ligand interactions and optical response of the material. A characteristic n–π* electronic transition was observed in the absorption spectrum of $Co_3V_2O_8$, manifested by a band at ~430 nm.[25,56,57] The E_g was extracted from the absorption data employing the equation $E_g = hc/\lambda_{max}$.[58] The E_g for $Co_3V_2O_8$ was determined to be 2.85 eV.[25] With the addition of PEG and PAA, absorption was enhanced in the visible region and a slight shift towards a longer wavelength (redshift) was observed, which reduces the E_g from 2.85 to 2.44 eV. E_g was calculated to be 2.72, 2.57, and 2.44 eV for PEG-$Co_3V_2O_8$, 2 wt% PAA/PEG-$Co_3V_2O_8$, and 4 wt% PAA/PEG-$Co_3V_2O_8$, respectively (Fig. S1).

Open Access Article. Published on 16 March 2026. Downloaded on 6/5/2026 2:20:00 AM.
This article is licensed under a Creative Commons Attribution-NonCommercial 3.0 Unported Licence.

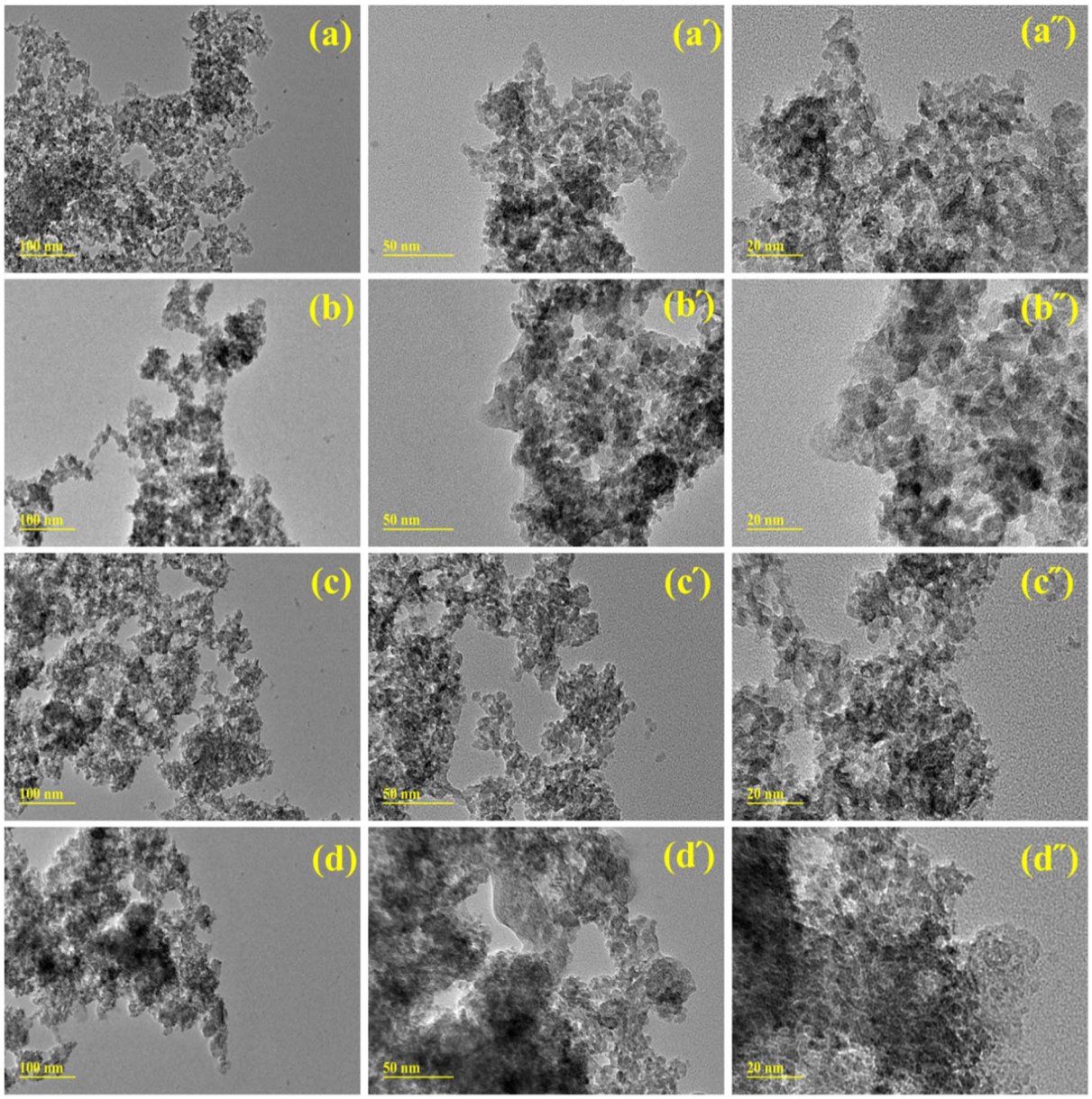

Fig. 4 (a–d″). TEM images at (a–d) 100 nm, (a′–d′) 50 nm, and (a″–d″) 20 nm of (a–a″) $Co_3V_2O_8$, (b–b″) 3 wt% PEG-$Co_3V_2O_8$, (c–c″) 2 wt% of PAA-doped PEG-$Co_3V_2O_8$, and (d–d″) 4 wt% of the PAA-doped PEG-$Co_3V_2O_8$ NPs.

TEM analysis was conducted to elucidate the morphological aspects of the synthesized samples. TEM micrograph reveals the agglomerated nanoparticles (NPs) of cobalt vanadate (Fig. 4a–a″). The addition of PEG (capping agent) formed a layer on the surface of NPs, resulting in the dispersion of NPs with no distinct morphology and reduced agglomeration, as evident from Fig. 4b–b″. Upon PAA incorporation, NPs agglomerate and this effect becomes more pronounced as the additive amount of PAA increases from 2 to 4 wt% (Fig. 4c and d″). Lattice spacings for the undoped and doped samples were found to be 0.253, 0.258, 0.260, and 0.262 nm, respectively, using the HR-TEM micrographs (Fig. S2). These results synchronized with the XRD data.

EDS was used to determine the elemental composition and purity of the synthesized NPs (Fig. S3(a–d)). Prominent peaks of cobalt (Co), vanadium (V), and oxygen (O) validate the successful synthesis of $Co_3V_2O_8$ (Fig. S3a). Additional carbon (C) peaks in Fig. S3b–d confirm the successful incorporation of the dopant species. Furthermore, Au peaks appearing in the spectra were attributed to the gold coating on the sample to minimize the charging effect (Fig. S3a–d). The elemental distribution of the synthesized NPs was assessed *via* mapping analysis, revealing uniform distributions of Co, V, O, and C elements in the highly doped specimen (Fig. S4a–e).

The combined effect of the reducing agent $NaBH_4$ and the prepared NCs in the RhB solution is crucial to the catalytic mechanism that involves electron transfer from $NaBH_4$ to RhB, resulting in dye degradation (Fig. S5). Without NCs, the reaction proceeds sluggishly. To overcome the energy barrier, a redox

© 2026 The Author(s). Published by the Royal Society of Chemistry

Open Access Article. Published on 16 March 2026. Downloaded on 6/5/2026 2:20:00 AM.
This article is licensed under a Creative Commons Attribution-NonCommercial 3.0 Unported Licence.

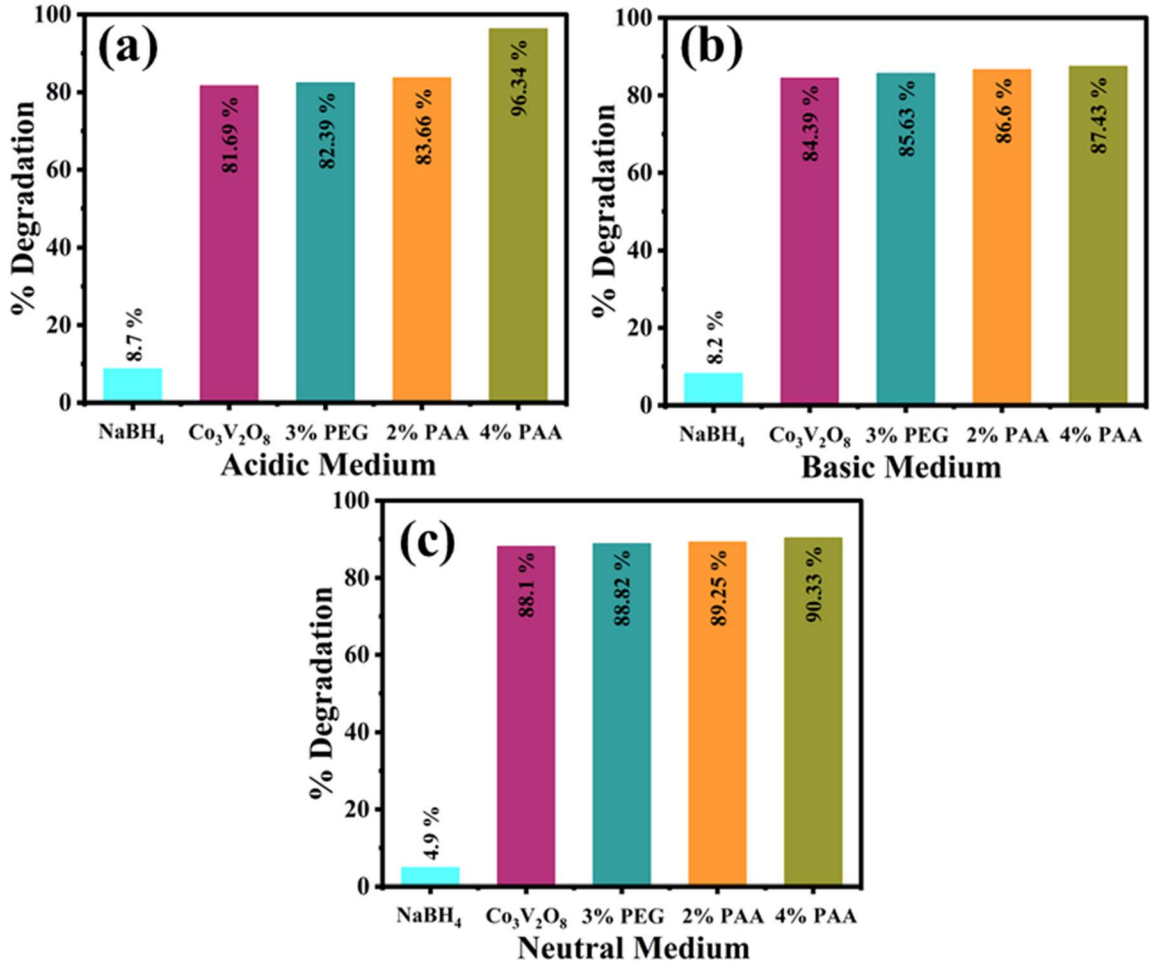

Fig. 5 Degradation efficacy of the undoped and doped NPs in (a) acidic, (b) basic, and (c) neutral media.

reaction involving $Co_3V_2O_8$ and PAA/PEG-doped $Co_3V_2O_8$ was added to accelerate the transfer of electrons between $NaBH_4$ and RhB. The NCs facilitate electron transfer, thereby accelerating the reaction kinetics. $NaBH_4$ dissociates into BH_4^- and Na^+ ions, with BH_4^- adsorbing onto the catalyst surface and releasing electrons that split it into H^+ ions. The NCs then channel electrons from BH_4^- to the RhB molecule. Subsequently, the H^+ attacks the dye molecule, breaking the π bonds within the dye and converting it into colorless RhB. The size and surface area of the catalyst facilitate abundant active sites, augmenting catalytic degradation when coupled with the reducing agent.

The degradation efficiency of the prepared NPs against RhB with $NaBH_4$ was assessed using a UV-Vis spectrophotometer. 0.5 M H_2SO_4 and 1 M NaOH were added to the RhB solution to stabilize the pH at ~2.5 and ~12, respectively. In the absence of a catalyst, the degradation efficacy was found to be 8.7%, 8.2%, and 4.9% in acidic, basic, and neutral media, respectively, as reported in our previous study.[59] The efficacy of $Co_3V_2O_8$, PEG-$Co_3V_2O_8$, 2 wt% of PAA/PEG-$Co_3V_2O_8$, and 4 wt% of PAA/PEG-$Co_3V_2O_8$ in degrading RhB was determined to be 81.69%, 82.39%, 83.66%, and 96.34% in acidic, 84.39%, 85.63%, 86.6%, and 87.43% in basic, and 88.1%, 88.82%, 89.25%, and 90.33% in neutral media within 10 minutes, respectively (Fig. 5). The pH of the solution essentially influences the degradation efficacy of the synthesized NCs. The pH determines the surface charges of the dye and catalysts and influences the catalytic activity. The maximum catalytic activity observed in the acidic medium is attributed to H^+ ions that adsorb readily on the catalyst surface. At low pH, the degradation efficacy increases, which is attributed to fast electron transfer and the extensive surface charge density of the catalyst.[60] Moreover, in acidic conditions (pH < 7), catalysts become positively charged; in contrast, RhB becomes negatively charged because of the ionization of the carboxyl (–COOH) group. This electrostatic interaction facilitates RhB reduction in an acidic medium.[61] In contrast, the increase in OH concentration in a basic environment is ascribed to the use of NaOH to increase the pH. This excess OH ions enhances degradation efficiency but also oxidizes the dye molecule. Additionally, excessive OH generation restricts the direct contact between dye molecules and catalysts, resulting in lower degradation efficacy compared to acidic medium. PEG enhances degradation in all media attributed to its unique structure and the ability to act as a hole scavenger, promoting charge separation and reducing the recombination of excitons.[62] With PAA addition, the increase in catalytic activity is

© 2026 The Author(s). Published by the Royal Society of Chemistry

Open Access Article. Published on 16 March 2026. Downloaded on 6/5/2026 2:20:00 AM.
This article is licensed under a Creative Commons Attribution-NonCommercial 3.0 Unported Licence.

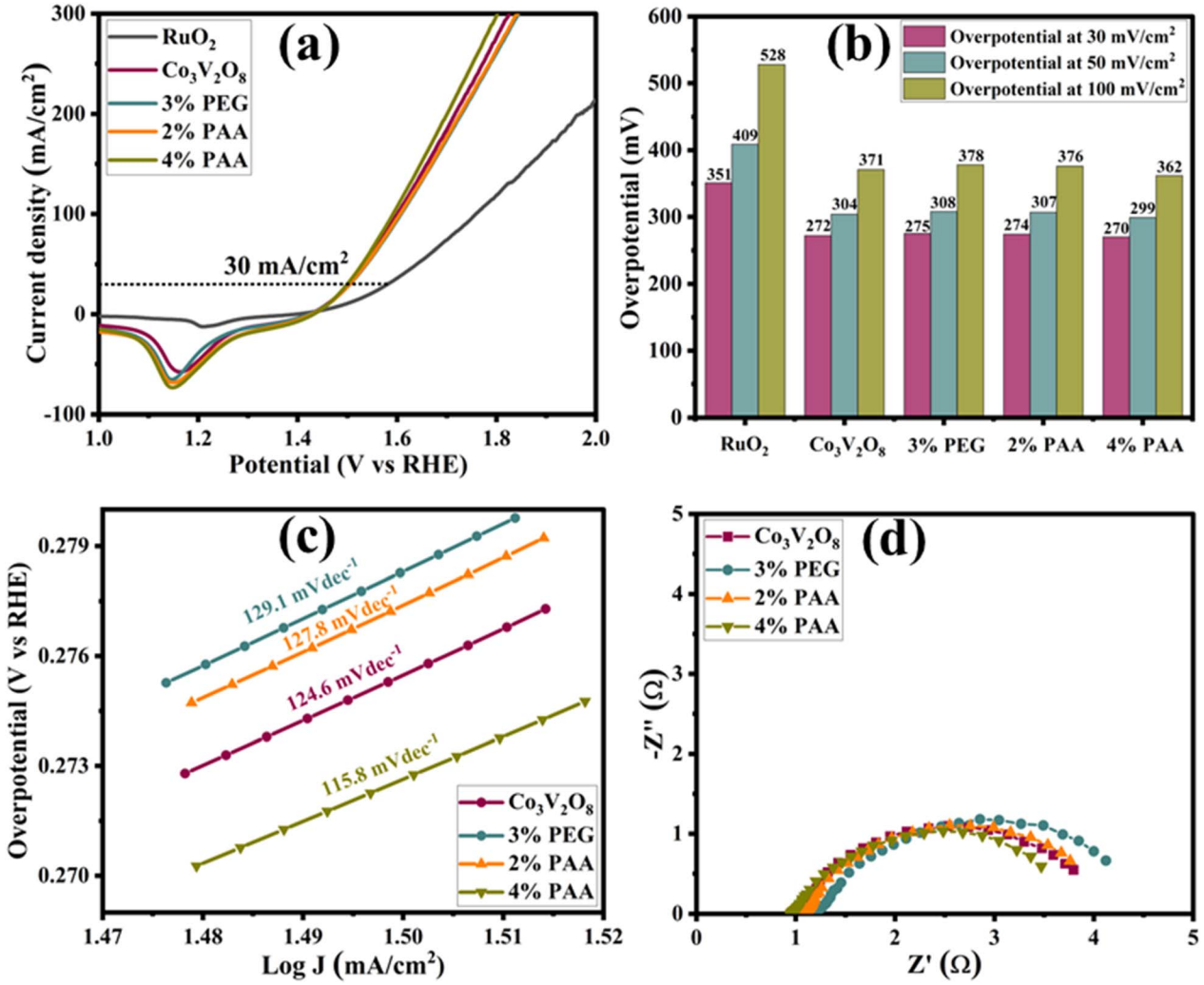

Fig. 6 (a) LSV polarization curve at a scan rate of 5 mV s^{-1}. (b) Bar graph showing the comparison of overpotential at current densities of 30, 50, and 100 mA cm^{-2}. (c) Tafel plots and (d) EIS Nyquist plots of the prepared electrocatalysts.

attributed to the decrease in the size of the NPs, which provides a larger surface area, thereby augmenting their degradation efficiency. Furthermore, the presence of carboxylic acid (–COOH) significantly enhanced the degradation by promoting electrostatic interactions.[63]

The intrinsic electrochemical activity of the prepared electrocatalysts, designated as $Co_3V_2O_8$, PEG-$Co_3V_2O_8$, 2% PAA/PEG-$Co_3V_2O_8$, and 4% PAA/PEG-$Co_3V_2O_8$, was determined by LSV. Voltammetric analysis was performed within the potential window of 1.0–2.0 V *vs.* RHE, and current density in response to the applied potential was monitored (Fig. 6a). Commercial RuO_2 was also assessed under the same parameters to serve as a benchmark electrocatalyst for comparative analysis, as previously reported (https://doi.org/10.1016/j.ijbiomac.2025.140433). Among all the tested electrocatalysts, the optimized sample (4% PAA/PEG-$Co_3V_2O_8$) demonstrates a superior OER activity requiring 270 mV @30 mA cm^{-2}. In contrast, PEG-$Co_3V_2O_8$ exhibits the highest overpotential of 275 mV to deliver a similar current density of 30 mA cm^{-2}. Moreover, the comparative analysis of overpotentials at 50 and 100 mV cm^{-2} shows that 4% PAA/PEG-$Co_3V_2O_8$ outperforms the other prepared electrocatalysts with the overpotentials of 299 and 362 mV to achieve the desired current density of 50 and 100 mA cm^{-2} (Fig. 6b). This highlights the role of PAA in enhancing the overall activity of $Co_3V_2O_8$. The overpotential of the prepared electrocatalysts is much lower than the benchmark RuO_2, which demonstrates 351, 409, and 528 mV at 30, 50, and 100 mA cm^{-2}, respectively. These findings unequivocally show the enhanced electrocatalytic activity of the prepared electrocatalyst relative to commercial RuO_2. With the incorporation of PAA, the observed lower shift in overpotential was attributed to the enhanced electronic conductivity and porous nature of the electrocatalyst.[35] Tafel slope is a pivotal kinetic parameter in evaluating the electrocatalytic activity of a catalyst, providing insights into reaction kinetics and activation energy associated with the OER. It predicts the change in the coupling transfer mechanism in electrons–protons and determines the rate of

© 2026 The Author(s). Published by the Royal Society of Chemistry

Open Access Article. Published on 16 March 2026. Downloaded on 6/5/2026 2:20:00 AM. This article is licensed under a Creative Commons Attribution-NonCommercial 3.0 Unported Licence.

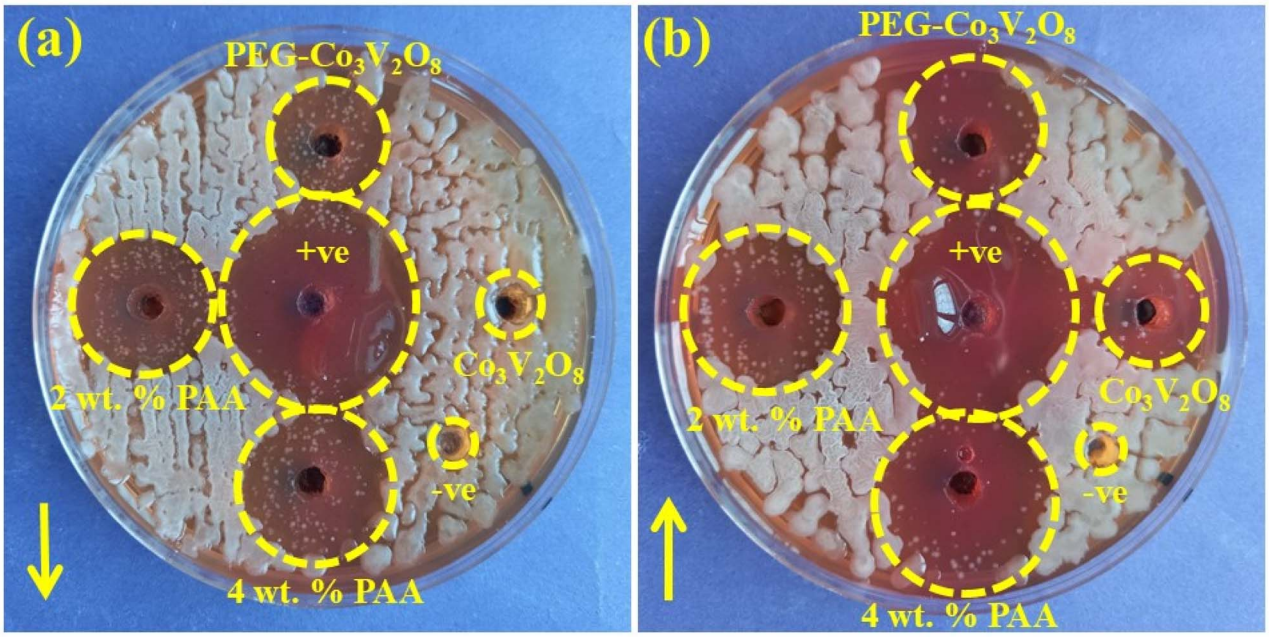

Fig. 7 *In vitro* antibacterial activity of the prepared NPs against MDR *S. aureus* at (a) minimum (b) and maximum concentrations.

increase in current density with applied potential. The smaller slope value suggests rapid reaction kinetics and improved activity. As shown in Fig. 6c, the optimized sample reveals a smaller Tafel slope of 115.8 mV dec^{-1} than $Co_3V_2O_8$ (124.6 mV dec^{-1}), PEG-$Co_3V_2O_8$ (129.1 mV dec^{-1}), and 2% PAA/PEG-Co_3V_2O (127.8 mV dec^{-1}). This indicates faster kinetics, corresponding to the lower activation energy barrier of the optimized sample at the electrode and electrolyte interface, consistent with a lower overpotential and high current density.[64] EIS was carried out to probe the electrochemical behavior, offering insights into reaction kinetics. The charge-transfer kinetics of the prepared electrocatalysts at the electrode–electrolyte interface were determined by the corresponding Nyquist plots, which are shown in Fig. 6d. The EIS fitting model for the prepared electrocatalyst displayed in Fig. S6 was used to compute the resistive parameters, as shown in (Table S1). All the prepared electrodes demonstrate Nyquist plots composed of semicircles, where the diameter of the semicircle corresponds to R_{ct} and the intercept at the *x*-axis was associated with equivalent series resistance (R_s). The R_{ct} reflects the ease of electron transfer at the interface (electrode–electrolyte), and R_s arises from the intrinsic resistance of the electrolyte (KOH). The optimized electrocatalyst exhibits a smaller semicircle diameter compared to other prepared electrocatalysts, suggesting rapid kinetics and enhanced electrical conductivity. The simulated values of R_s and R_{ct} of the prepared electrodes show that the 4% PAA/PEG-$Co_3V_2O_8$ exhibits the smallest R_s (0.969 Ω) and R_{ct} (3.02 Ω), as detailed in Table S1. This reduced interfacial charge-transfer resistance contributes to its minimal overpotential and Tafel slope. The LSV, Tafel slope, and EIS analysis show that the optimized sample exhibits the highest electrocatalytic activity among other prepared samples, affirming its superior OER activity.

The agar well diffusion technique was used to evaluate the *in vitro* antibacterial activity of the prepared NPs against MDR *S. aureus* by measuring the inhibition zones (mm) depicted in Fig. 7, S7 and S8. The zones against MDR *S. aureus* were measured at low (0.5 mg/50 μL) and high (1.0 mg/50 μL) concentrations (Table 1). The zone ranges were determined to be 1.65 ± 0.15 to 6.95 ± 0.82 mm and 4.75 ± 0.42 to 8.25 ± 0.93 mm for the low and high dosages, respectively. The acquired results were assessed in correlation with the positive control CIP (10.55 ± 0.08 mm) and negative control DI water (0 ± 0.00 mm). The results demonstrated that the undoped sample exhibited the smallest inhibition diameter. In contrast, the highly doped sample showed maximum inhibition diameter at both concentrations, indicating significant potential of NPs against MDR *S. aureus*.

Transition metal oxides encourage ROS generation, attributed to their hydrophobic and electrostatic interactions with surface water and hydroxyl groups, thereby exhibiting significant antibacterial activity. These generated ROS induce oxidative stress and disrupt the bacterial cell wall. The oxidative stress is influenced by the size and concentration of the NPs. Smaller particles generate higher ROS, including H_2O_2,

Table 1 Antibacterial activity of PAA/PEG-$Co_3V_2O_8$

Material	Inhibition zone (mm) (0.5 mg/50 μL)	Inhibition zone (mm) (1.0 mg/50 μL)
$Co_3V_2O_8$	1.65 ± 0.15	4.75 ± 0.42
PEG-$Co_3V_2O_8$	4.85 ± 0.44	6.65 ± 0.65
2 wt% PAA	6.05 ± 0.64	7.45 ± 0.87
4 wt% PAA	6.95 ± 0.82	8.25 ± 0.93
CIP	10.55 ± 0.08	10.55 ± 0.08
DI water	0 ± 0.00	0 ± 0.00

© 2026 The Author(s). Published by the Royal Society of Chemistry

Open Access Article. Published on 16 March 2026. Downloaded on 6/5/2026 2:20:00 AM.
This article is licensed under a Creative Commons Attribution-NonCommercial 3.0 Unported Licence.

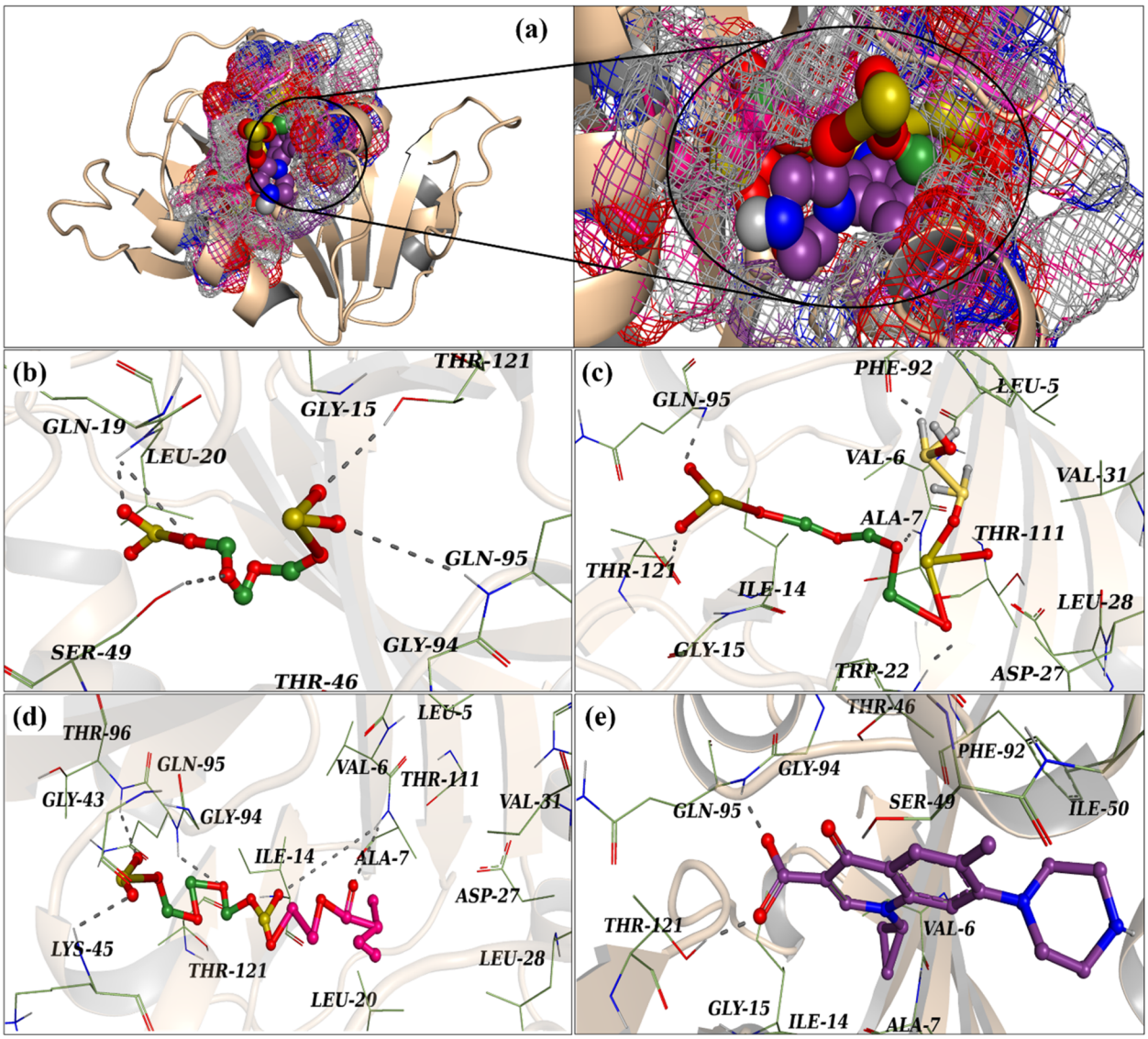

Fig. 8 Binding interaction within the active site of DHFR$_{S.\ aureus}$: superimposed ligands (a), $Co_3V_2O_8$ (b), PEG-$Co_3V_2O_8$ NPs (c), PAA/PEG-$Co_3V_2O_8$ NPs (d), and ciprofloxacin (e).

superoxide ($O_2^{\bullet}$), and OH radicals. These ROS disrupt the bacterial membrane, resulting in the release of cytoplasmic components and eventually leading to bacterial cell destruction. The electron–hole pair directly influences the generation of ROS and exerts a detrimental effect on bacterial cells, ultimately rupturing the cell membrane. The synthesized NPs interact with bacterial cells, disrupting the membrane integrity and causing the leakage of cellular components, resulting in cell death (Fig. S9).[65–68] $Co_3V_2O_8$ demonstrates significant antibacterial activity attributed to the presence of cobalt ions that binds with the thiol group and disrupts enzymatic functions. These Co^{2+} ions influence bacterial membrane integrity due to electrostatic interactions and substantially increase ROS production, especially H_2O_2, leading to bacterial cell death.[24] The antibacterial activity is enhanced with PEG, attributed to the synergistic effect between $Co_3V_2O_8$ and PEG. PEG contains carbonyl groups, which enhance penetration, and consequently increase its efficacy in inhibiting bacterial growth.[69] The PAA inclusion resulted in enlarged inhibitory zones and increased antibacterial activity, facilitating ROS formation *via* its carboxylic and hydroxyl groups.[70] The addition of polymers (PEG and PAA) reduces the crystallite size, enhances active sites and promotes ROS generation, thereby improving antimicrobial activity.

Molecular docking was employed as a qualitative modeling approach to explore probable inhibitory effects of the synthesized NPs on bacterial enzyme DHFR from *Staphylococcus aureus* (Fig. 8a). The enzyme DHFR is ubiquitous across all cellular structures and plays a crucial role in sustaining intracellular folate reserves in a biochemically active reduced form. DHFR catalyzes the reduction of dihydrofolate to tetrahydrofolate and in the synthesis of amino acids, purines, and thymidylate. Inhibitors of DHFR have the capacity to impede the synthesis of DNA, RNA, and proteins, thereby halting cellular proliferation. The intricate $Co_3V_2O_8$ NPs exhibited

© 2026 The Author(s). Published by the Royal Society of Chemistry

Open Access Article. Published on 16 March 2026. Downloaded on 6/5/2026 2:20:00 AM.
This article is licensed under a Creative Commons Attribution-NonCommercial 3.0 Unported Licence.

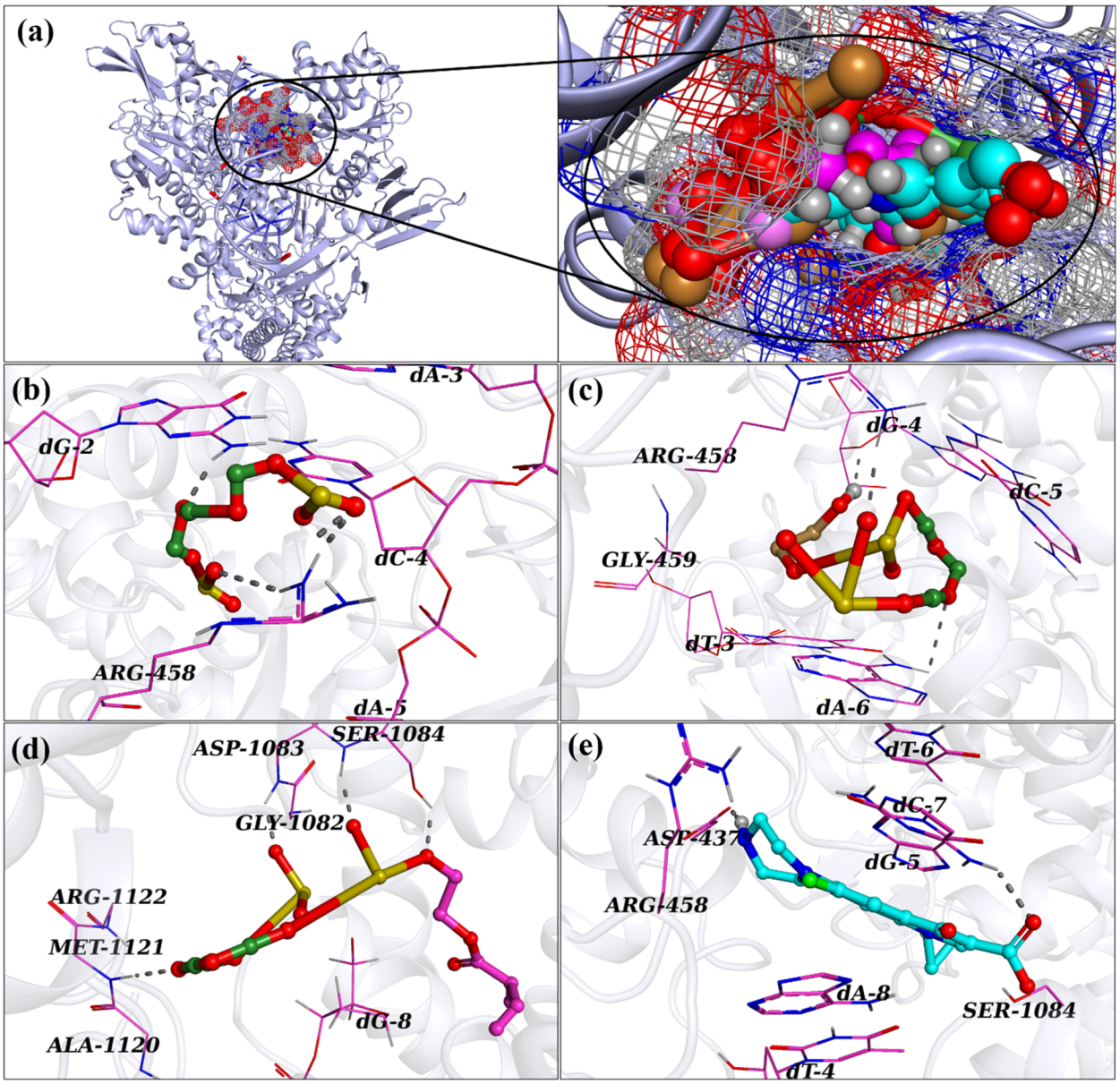

Fig. 9 Binding interactions within the active site of topoisomerase II in DNA gyrase$_{S.\ aureus}$: superimposed ligands (a), $Co_3V_2O_8$ (b), PEG-$Co_3V_2O_8$ NPs (c), PAA/PEG-$Co_3V_2O_8$ NPs (d), and ciprofloxacin (e).

a binding score of 5.23, indicating significant binding interactions with essential amino acid residues within the active site, by forming hydrogen bonds with Gly15, Gln95, Leu20, and Gly94 (Fig. 8b). PEG-$Co_3V_2O_8$ NPs demonstrated a binding score of 6.24, indicating significant binding interactions with Gln95, Phe92, Thr121, and Trp22 (Fig. 8c). Similar to ciprofloxacin, which demonstrates a standard score of 7.26 and participates in hydrogen bonding with Thr121 and Gln95 (Fig. 8e), the binding score of 8.62 for the PAA/PEG-$Co_3V_2O_8$ NPs indicates a multifaceted interaction that involves hydrogen bonds with Gly94, Lys45, Ala7, and Thr121 (Fig. 8d and Table S2).

The gyrase enzyme is integral for DNA replication, as it cleaves both strands of supercoiled DNA, interweaves them, and subsequently reseals them, facilitating the unwinding of DNA necessary for replication. The evaluation of the synthesized NPs in their capacity to inhibit the activity of topoisomerase II enzyme, identified as a promising molecular target, was conducted in conjunction with ciprofloxacin, serving as a reference compound. The molecular modelling of the co-crystallized ligand elucidated interactions within the active site of topoisomerase II enzyme, including hydrogen bonding and pi–cationic interactions with the DNA nucleotide base (Fig. 9a). The $Co_3V_2O_8$ NPs demonstrate a binding score of 3.57, signifying hydrogen bonds with Arg458 (Fig. 9b). The PEG-$Co_3V_2O_8$ NPs exhibited a binding score of 4.23 in Fig. 9c. Similar to ciprofloxacin having a standard score of 6.73 and participates in conventional hydrogen bonding with Asp43 (Fig. 9e), whereas a binding score of 4.74 for PAA/PEG-$Co_3V_2O_8$ NPs indicates

Open Access Article. Published on 16 March 2026. Downloaded on 6/5/2026 2:20:00 AM. This article is licensed under a Creative Commons Attribution-NonCommercial 3.0 Unported Licence.

hydrogen bonds with Met1121, Gly1082, Ser1084, and Asp1083 (Fig. 9d and Table S3). The docking models illustrate basic inorganic–polymer clusters and may not fully capture the comprehensive aggregation state seen in experimental observations. Consequently, the docking scores are not intended to represent quantitative binding affinities or enable direct comparisons with small-molecule antibiotics. The docking data are provided as qualitative, supporting evidence of possible interaction tendencies. These data indicate that surface functionalization may affect enzyme–nanoparticle interactions and underscore the necessity for experimental validation to verify antibacterial processes.

4. Conclusion

In this study, an environmentally benign coprecipitation route was employed to fabricate $Co_3V_2O_8$ and polymer (PEG and PAA) doped $Co_3V_2O_8$ NPs. The objective of this study is to assess the catalytic potential, OER activity, and antimicrobial efficacy of NPs against *S. aureus*. XRD revealed the orthorhombic phase of $Co_3V_2O_8$ NPs. The polycrystalline nature of the synthesized NPs was verified by SAED analysis. FTIR endorsed the V═O symmetrical stretching vibration at 933 cm^{-1} and Co–O and V–O–V bond vibrations at 561 cm^{-1}. The PAA and PEG insertion enhanced the absorption capability, which consequently reduced the E_g from 2.85 to 2.44 eV. TEM elucidates the formation of NPs of $Co_3V_2O_8$ and agglomeration was observed with the incorporation of polymers. Additionally, EDS and mapping further verified the successful synthesis of PAA/PEG-$Co_3V_2O_8$ NPs by assessing their elemental composition. The doped materials exhibit superior activity compared to the pristine sample in RhB degradation, OER activity, and antibacterial performance against *S. aureus*. The 4 wt% of PAA/PEG-$Co_3V_2O_8$ NPs outperformed the other samples, achieving the maximum degradation of 96.33% in an acidic medium and remarkable antibacterial efficacy with a zone of 8.25 ± 0.93 mm. Similarly, the optimized electrocatalyst showed a superior OER activity with the minimal overpotential of 270, 299, and 362 mV at 30, 50, 100 mA cm^{-2} respectively, lowest Tafel slope, and R_{ct}. Computational investigations demonstrated that these NPs may serve as potential inhibitors of topoisomerase II and DHFR in *S. aureus*. These findings highlight the potential of the polymer (PAA and PEG)-modified $Co_3V_2O_8$ NPs as an efficient multifunctional catalyst.

Conflicts of interest

The authors declare that they have no known competing financial interests or personal relationships that could have appeared to influence the work reported in this paper.

Data availability

The original contributions presented in this study are included in the article. Further inquiries can be directed to the corresponding author. The first author completed her research work under the supervision of the second author (currently in KFUPM).

Supplementary information (SI) is available. See DOI: https://doi.org/10.1039/d5na01130b.

Acknowledgements

Authors from Pakistan are grateful to the higher education commission (HEC), Pakistan, for supporting this work through grant NRPU-20-17615 (Muhammad Ikram, PI). The authors also extend their appreciation to the Deanship of Research and Graduate Studies at King Khalid University for funding this work through the Large Groups Project under grant number (RGP.2/474/46).

References

1 H. Kumari, S. Sonia, R. Ranga, S. Chahal, S. Devi, S. Sharma, S. Kumar, P. Kumar and S. Kumar, A review on photocatalysis used for wastewater treatment: dye degradation, *Water, Air, Soil Pollut.*, 2023, **234**, 349.
2 M. Ge, N. Zhu, Y. Zhao, J. Li and L. Liu, Sunlight-assisted degradation of dye pollutants in Ag3PO4 suspension, *Ind. Eng. Chem. Res.*, 2012, **51**, 5167–5173.
3 L. Liu, B. Zhang, Y. Zhang, Y. He, L. Huang, S. Tan and X. Cai, Simultaneous removal of cationic and anionic dyes from environmental water using montmorillonite-pillared graphene oxide, *J. Chem. Eng. Data*, 2015, **60**, 1270–1278.
4 M. Hasnat, I. Siddiquey and A. Nuruddin, Comparative photocatalytic studies of degradation of a cationic and an anionic dye, *Dyes Pigm.*, 2005, **66**, 185–188.
5 Y. Yue, K. Hou, J. Chen, W. Cheng, Q. Wu, J. Han and J. Jiang, Ag/AgBr/$AgVO_3$ photocatalyst-embedded polyacrylonitrile/polyamide/chitosan nanofiltration membrane for integrated filtration and degradation of RhB, *ACS Appl. Mater. Interfaces*, 2022, **14**, 24708–24719.
6 H. Lee, S. H. Park, Y.-K. Park, B. H. Kim, S.-J. Kim and S.-C. Jung, Rapid destruction of the rhodamine B using TiO_2 photocatalyst in the liquid phase plasma, *Chem. Cent. J.*, 2013, **7**, 1–5.
7 G. Centi, P. Ciambelli, S. Perathoner and P. Russo, Environmental catalysis: trends and outlook, *Catal. Today*, 2002, **75**, 3–15.
8 S. Hyun, V. Ahilan, H. Kim and S. Shanmugam, The influence of $Co_3V_2O_8$ morphology on the oxygen evolution reaction activity and stability, *Electrochem. Commun.*, 2016, **63**, 44–47.
9 M. El-Shafie, Hydrogen production by water electrolysis technologies: A review, *Results Eng.*, 2023, **20**, 101426.
10 M. A. Khan, H. Zhao, W. Zou, Z. Chen, W. Cao, J. Fang, J. Xu, L. Zhang and J. Zhang, Recent progresses in electrocatalysts for water electrolysis, *Electrochem. Energy Rev.*, 2018, **1**, 483–530.
11 K. Wu, C. Lyu, J. Cheng, Z. Guo, H. Li, X. Zhu, W. M. Lau and J. Zheng, Modulating electronic structure by etching strategy to construct $NiSe_2/Ni_{0.85}Se$ heterostructure for urea-assisted hydrogen evolution reaction, *Small*, 2024, **20**, 2304390.
12 S. A. Pawar, S. V. Talekar, P. D. Sawant, S. P. Patole, H. M. Yadav and J. L. Gunjakar, 2D-1D Self-Assembly of

 © 2026 The Author(s). Published by the Royal Society of Chemistry

Open Access Article. Published on 16 March 2026. Downloaded on 6/5/2026 2:20:00 AM. This article is licensed under a Creative Commons Attribution-NonCommercial 3.0 Unported Licence.

Water Delaminated Co-Fe-LDH Nanosheets and CNTs via Exfoliation-Restacking Approach for Efficient Oxygen Evolution Reaction, *Small*, 2025, e06554.

13 Z. Chen, X. Duan, W. Wei, S. Wang and B.-J. Ni, Iridium-based nanomaterials for electrochemical water splitting, *Nano Energy*, 2020, **78**, 105270.

14 N. L. Maia, M. De Barros, L. L. De Oliveira, S. A. Cardoso, M. H. Dos Santos, F. A. Pieri, T. C. Ramalho, E. F. Da Cunha and M. A. Moreira, Synergism of plant compound with traditional antimicrobials against Streptococcus spp. isolated from bovine mastitis, *Front. Microbiol.*, 2018, **9**, 1203.

15 A. Haider, M. Ijaz, S. Ali, J. Haider, M. Imran, H. Majeed, I. Shahzadi, M. M. Ali, J. A. Khan and M. Ikram, Green synthesized phytochemically (Zingiber officinale and Allium sativum) reduced nickel oxide nanoparticles confirmed bactericidal and catalytic potential, *Nanoscale Res. Lett.*, 2020, **15**, 1–11.

16 A. Girma and D. Tamir, Prevalence of bovine mastitis and its associated risk factors among dairy cows in Ethiopia during 2005–2022: a systematic review and meta-analysis, *Vet. Med. Int.*, 2022, **2022**, 7775197.

17 Q. Xu, W. Qin and J.-F. Chu, Novel $Co_{3(1-x)}$ Fe_{3x} V_2O_8 Nanoparticles as Highly Active and Noble-Metal-Free Electrocatalysts for Oxygen Evolution Reaction, *Energy Fuels*, 2020, **34**, 15019–15025.

18 Y. Teng, Y. Li, D. Yu, Y. N. Meng, Y. Wu, X. Zhao and X. Liu, The Microwave-Assisted Hydrothermal Synthesis of CoV_2O_6 and $Co_3V_2O_8$ with Morphology Tuning by pH Adjustments for Supercapacitor Applications, *ChemistrySelect*, 2019, **4**, 956–962.

19 G. Yang, H. Cui, G. Yang and C. Wang, Self-assembly of $Co_3V_2O_8$ multilayered nanosheets: controllable synthesis, excellent Li-storage properties, and investigation of electrochemical mechanism, *ACS Nano*, 2014, **8**, 4474–4487.

20 Y. Zhao, Y. Liu, X. Du, R. Han and Y. Ding, Hexagonal assembly of $Co_3V_2O_8$ nanoparticles acting as an efficient catalyst for visible light-driven water oxidation, *J. Mater. Chem. A*, 2014, **2**, 19308–19314.

21 M. M. Sajid, N. Amin, N. A. Shad, Y. Javed and Z. Zhang, Hydrothermal fabrication of monoclinic bismuth vanadate (m-$BiVO_4$) nanoparticles for photocatalytic degradation of toxic organic dyes, *Mater. Sci. Eng., B*, 2019, **242**, 83–89.

22 T. Li, L. Zhao, Y. He, J. Cai, M. Luo and J. Lin, Synthesis of g-C_3N_4/$SmVO_4$ composite photocatalyst with improved visible light photocatalytic activities in RhB degradation, *Appl. Catal., B*, 2013, **129**, 255–263.

23 X. Hu and C. Hu, Preparation and visible-light photocatalytic activity of Ag3VO4 powders, *J. Solid State Chem.*, 2007, **180**, 725–732.

24 A. Simo, M. Drah, N. Sibuyi, M. Nkosi, M. Meyer and M. Maaza, Hydrothermal synthesis of cobalt-doped vanadium oxides: Antimicrobial activity study, *Ceram. Int.*, 2018, **44**, 7716–7722.

25 M. Ghiyasiyan-Arani and M. Masjedi-Arani, Size controllable synthesis of cobalt vanadate nanostructures with enhanced photocatalytic activity for the degradation of organic dyes, *J. Mol. Catal. A: Chem.*, 2016, **425**, 31–42.

26 S. S. Saeidi, P. Sanati, G. Rezaei and B. Vaseghi, Synthesis and improving antibacterial effectiveness of Ag/$Co_3V_2O_8$ nanocomposites by graphene oxide for biomedical applications, *Mater. Sci. Eng., B*, 2024, **306**, 117457.

27 F. Ahmadi, M. Rahimi-Nasrabadi, M. Daneshmehr and M. Eghbali-Arani, Synthesis, characterization, and investigation of magnetic, photocatalytic and antibacterial properties of TbVO 4 nanoparticles, *J. Mater. Sci.: Mater. Electron.*, 2017, **28**, 14362–14368.

28 M. Anandan, S. Dinesh, N. Krishnakumar and K. Balamurugan, Improved photocatalytic properties and anti-bacterial activity of size reduced ZnO nanoparticles via PEG-assisted precipitation route, *J. Mater. Sci.: Mater. Electron.*, 2016, **27**, 12517–12526.

29 H. Chang, E.-H. Jo, H. D. Jang and T.-O. Kim, Synthesis of PEG-modified TiO2–InVO4 nanoparticles via combustion method and photocatalytic degradation of methylene blue, *Mater. Lett.*, 2013, **92**, 202–205.

30 S. Moradi, M. Vossoughi, M. Feilizadeh, S. M. E. Zakeri, M. M. Mohammadi, D. Rashtchian and A. Yoosefi Booshehri, Photocatalytic degradation of dibenzothiophene using La/PEG-modified TiO 2 under visible light irradiation, *Res. Chem. Intermed.*, 2015, **41**, 4151–4167.

31 S. Elhag, D. Tordera, T. Deydier, J. Lu, X. LiU, V. Khranovskyy, L. Hultman, M. Willander, M. Jonsson and O. Nur, Low-temperature growth of polyethylene glycol-doped $BiZn_2VO_6$ nanocompounds with enhanced photoelectrochemical properties, *J. Mater. Chem. A*, 2017, **5**, 1112–1119.

32 A. Kausar, Poly (acrylic acid) nanocomposites: Design of advanced materials, *J. Plast. Film Sheeting*, 2021, **37**, 409–428.

33 Y. Tang, Y. Li, Y. Zhang, C. Mu, J. Zhou, W. Zhang and B. Shi, Nonswelling silica–poly (acrylic acid) composite for efficient and simultaneous removal of cationic dye, heavy metal, and surfactant-stabilized emulsion from wastewater, *Ind. Eng. Chem. Res.*, 2020, **59**, 3383–3393.

34 M. Bhosale, P. J. Morankar, Y. Lee, H. Seo and C.-W. Jeon, Electropolymerized PAA as a Functional Matrix for CeO2-NiO Hybrid Electrocatalysts for Efficient Water Oxidation, *Polymers*, 2025, **17**, 2631.

35 P. Panneerselvam, C. Singh, S. K. Jayaraj, T. Doulassiramane, R. Padmanaban, A. K. Samal, S. Mohan and A. H. Jadhav, Unveiling the impact of oxygen vacancies in engineered bimetallic oxides for enhanced oxygen evolution reaction: insights from experimental and theoretical approaches, *J. Mater. Chem. A*, 2024, **12**, 19149–19167.

36 M. R. Shaik, M. Kuniyil, M. Khan, N. Ahmad, A. Al-Warthan, M. R. H. Siddiqui and S. F. Adil, Modified polyacrylic acid-zinc composites: Synthesis, characterization and biological activity, *Molecules*, 2016, **21**, 292.

37 I. Urooj, M. Noor, W. A. Shah, M. Arfan, M. A. Wahab, A. Abdala and M. Sohail, Solid-State Engineered Fe-CoMoO4 with a Defect-Rich Structure: Trimetallic Synergy

Open Access Article. Published on 16 March 2026. Downloaded on 6/5/2026 2:20:00 AM. This article is licensed under a Creative Commons Attribution-NonCommercial 3.0 Unported Licence.

for Enhanced Oxygen Evolution Reaction, *Energy Fuels*, 2025, **39**(36), 17651–17660.
38 D. H. Bergey, *Bergey's Manual of Determinative Bacteriology*, Lippincott Williams & Wilkins, 1994.
39 A. Bauer, W. Kirby, J. C. Sherris and M. Turck, Antibiotic susceptibility testing by a standardized single disk method, *Am. J. Clin. Pathol.*, 1966, **45**, 493–496.
40 F. Adzitey, S. Yussif, R. Ayamga, S. Zuberu, F. Addy, G. Adu-Bonsu, N. Huda and R. Kobun, Antimicrobial susceptibility and molecular characterization of Escherichia coli recovered from milk and related samples, *Microorganisms*, 2022, **10**, 1335.
41 I. Lewis and S. James, *Performance Standards for Antimicrobial Susceptibility Testing*, 2022.
42 B. Iwalokun, A. Ogunledun, D. Ogbolu, S. Bamiro and J. Jimi-Omojola, In vitro antimicrobial properties of aqueous garlic extract against multidrug-resistant bacteria and Candida species from Nigeria, *J. Med. Food*, 2004, **7**, 327–333.
43 P. Rayam, N. Polkam, N. Kuntala, V. Banothu, H. S. Anantaraju, Y. Perumal, S. Balasubramanian and J. S. Anireddy, Design and synthesis of oxaprozin-1, 3, 4-oxadiazole hybrids as potential anticancer and antibacterial agents, *J. Heterocycl. Chem.*, 2020, **57**, 1071–1082.
44 F. Nazzaro, G. Caliendo, G. Arnesi, A. Veronesi, P. Sarzi and F. Fratianni, Comparative content of some bioactive compounds in two varieties of Capsicum annuum L. sweet pepper and evaluation of their antimicrobial and mutagenic activities, *J. Food Biochem.*, 2009, **33**, 852–868.
45 I. Shahzadi, M. Islam, H. Saeed, A. Haider, A. Shahzadi, J. Haider, N. Ahmed, A. Ul-Hamid, W. Nabgan and M. Ikram, Formation of biocompatible MgO/cellulose grafted hydrogel for efficient bactericidal and controlled release of doxorubicin, *Int. J. Biol. Macromol.*, 2022, **220**, 1277–1286.
46 B. D. Bax, P. F. Chan, D. S. Eggleston, A. Fosberry, D. R. Gentry, F. Gorrec, I. Giordano, M. M. Hann, A. Hennessy and M. Hibbs, Type IIA topoisomerase inhibition by a new class of antibacterial agents, *Nature*, 2010, **466**, 935–940.
47 C. Oefner, S. Parisi, H. Schulz, S. Lociuro and G. E. Dale, Inhibitory properties and X-ray crystallographic study of the binding of AR-101, AR-102 and iclaprim in ternary complexes with NADPH and dihydrofolate reductase from Staphylococcus aureus, *Acta Crystallogr., Sect. D: Biol. Crystallogr.*, 2009, **65**, 751–757.
48 W. H. Low, C. W. Siong, C. H. Chia, S. S. Lim and P. S. Khiew, A facile synthesis of graphene/$Co_3V_2O_8$ nanocomposites and their enhanced charge storage performance in electrochemical capacitors, *J. Sci.: Adv. Mater. Devices*, 2019, **4**, 515–523.
49 M. B. Ahmad, M. Y. Tay, K. Shameli, M. Z. Hussein and J. J. Lim, Green synthesis and characterization of silver/chitosan/polyethylene glycol nanocomposites without any reducing agent, *Int. J. Mol. Sci.*, 2011, **12**, 4872–4884.
50 R. L. Naik, T. B. Narsaiah, P. Justin, A. N. Kumar, M. Somashekar, N. Raghavendra, C. Ravikumar, A. A. Khan and M. Santosh, Hydrothermally synthesized cobalt vanadate nanoparticles for photocatalytic degradation of Fast Orange Red dye and supercapacitor applications, *Mater. Sci. Eng., B*, 2023, **298**, 116861.
51 L. R. Naik, P. Justin and T. B. Narsaiah, Controllable synthesis of cobalt vanadate nanostructure materials for direct methanol fuel cell applications, *Proceedings of the International Conference on Advances in Chemical Engineering (AdChE)*, 2020.
52 L. Zhang, S. Chang, X. Lu, T. Han, R. Jin, T. Zhao, D. Fang, M. Xie, M. Wang and J. Yi, Vapor phosphorus-coated cobalt vanadate as a high-performance anode for a lithium-ion battery, *J. Solid State Electrochem.*, 2022, **26**, 917–927.
53 R. L. Naik, T. B. Narsaiah and P. Justin, Hydrothermal synthesis and characterization of cobalt vanadate nanoparticles for supercapacitor applications, *Mater. Today: Proc.*, 2023, DOI: 10.1016/j.matpr.2023.05.725.
54 A. M. Ali, N. A. Ghazwani, H. Algarni and A. A. Ismail, Synthesis of ZnO–SnO_2 nanocomposites: impact of polyethylene glycol on morphological, luminescence and photocatalytic properties, *Res. Chem. Intermed.*, 2019, **45**, 3089–3106.
55 A. Jose, K. R. Sunaja Devi, D. Pinheiro and S. Lakshmi Narayana, Electrochemical synthesis, photodegradation and antibacterial properties of PEG capped zinc oxide nanoparticles, *J. Photochem. Photobiol., B*, 2018, **187**, 25–34.
56 K. Skrabania, A. Miasnikova, A. M. Bivigou-Koumba, D. Zehm and A. Laschewsky, Examining the UV-vis absorption of RAFT chain transfer agents and their use for polymer analysis, *Polym. Chem.*, 2011, **2**, 2074–2083.
57 S. E. Arasi, R. Ranjithkumar, P. Devendran, M. Krishnakumar and A. Arivarasan, Studies on electrochemical mechanism of nanostructured cobalt vanadate electrode material for pseudocapacitors, *J. Energy Storage*, 2021, **41**, 102986.
58 R. N. Ali, H. Naz, J. Li, X. Zhu, P. Liu and B. Xiang, Band gap engineering of transition metal (Ni/Co) codoped in zinc oxide (ZnO) nanoparticles, *J. Alloys Compd.*, 2018, **744**, 90–95.
59 M. Imran, A. Haider, I. Shahzadi, S. Moeen, A. Ul-Hamid, W. Nabgan, A. Shahzadi, T. Alshahrani and M. Ikram, Polyvinylpyrrolidone and chitosan-coated magnetite (Fe_3O_4) nanoparticles for catalytic and antimicrobial activity with molecular docking analysis, *J. Environ. Chem. Eng.*, 2023, **11**, 110088.
60 H.-J. Cui, H.-Z. Huang, B. Yuan and M.-L. Fu, Decolorization of RhB dye by manganese oxides: effect of crystal type and solution pH, *Geochem. Trans.*, 2015, **16**, 10.
61 T. S. Natarajan, M. Thomas, K. Natarajan, H. C. Bajaj and R. J. Tayade, Study on UV-LED/TiO_2 process for degradation of Rhodamine B dye, *Chem. Eng. J.*, 2011, **169**, 126–134.
62 A. Laouini, A. Bouafia, S. E. Laouini, H. A. Mohammed, M. L. Tedjani, F. Alharthi and J. A. A. Abdullah, Boosted Antioxidant and Photocatalytic Power: Reusable PEG-Coated Iron Oxide Nanocomposites for Effective

© 2026 The Author(s). Published by the Royal Society of Chemistry

Open Access Article. Published on 16 March 2026. Downloaded on 6/5/2026 2:20:00 AM.
This article is licensed under a Creative Commons Attribution-NonCommercial 3.0 Unported Licence.

Cephalexin and BCB Dye Degradation, *J. Cluster Sci.*, 2024, 1–21.

63 F. Jamal, M. Ikram, A. Haider, A. Ul-Hamid, M. Ijaz, W. Nabgan, J. Haider and I. Shahzadi, Facile synthesis of silver and polyacrylic acid doped magnesium oxide nanostructure for photocatalytic dye degradation and bactericidal behavior, *Appl. Nanosci.*, 2022, **12**, 2409–2419.

64 A. Alobaid, C. Wang and R. A. Adomaitis, Mechanism and Kinetics of HER and OER on NiFe LDH Films in an Alkaline Electrolyte, *J. Electrochem. Soc.*, 2018, **165**, J3395–J3404.

65 P. Hosseinkhani, A. Zand, S. Imani, M. Rezayi and S. Rezaei Zarchi, Determining the antibacterial effect of ZnO nanoparticle against the pathogenic bacterium, Shigella dysenteriae (type 1), *Int. J. Nano Dimens.*, 2011, **1**, 279–285.

66 B. Ahmed, B. Solanki, A. Zaidi, M. S. Khan and J. Musarrat, Bacterial toxicity of biomimetic green zinc oxide nanoantibiotic: insights into ZnONP uptake and nanocolloid–bacteria interface, *Toxicol. Res.*, 2019, **8**, 246–261.

67 K. Ali, B. Ahmed, S. M. Ansari, Q. Saquib, A. A. Al-Khedhairy, S. Dwivedi, M. Alshaeri, M. S. Khan and J. Musarrat, Comparative in situ ROS mediated killing of bacteria with bulk analogue, Eucalyptus leaf extract (ELE)-capped and bare surface copper oxide nanoparticles, *Mater. Sci. Eng., C*, 2019, **100**, 747–758.

68 S. M. Dizaj, F. Lotfipour, M. Barzegar-Jalali, M. H. Zarrintan and K. Adibkia, Antimicrobial activity of the metals and metal oxide nanoparticles, *Mater. Sci. Eng., C*, 2014, **44**, 278–284.

69 M. Jayanetti, C. Thambiliyagodage, H. Liyanaarachchi, G. Ekanayake, A. Mendis and L. Usgodaarachchi, In vitro influence of PEG functionalized ZnO–CuO nanocomposites on bacterial growth, *Sci. Rep.*, 2024, **14**, 1293.

70 H. Shahzad, M. Imran, A. Haider, S. Naz, E. Umar, A. Ul-Hamid, W. Nabgan, M. M. Algaradah, A. M. Fouda and J. Haider, Catalytic and antimicrobial properties of Ag and polyacrylic acid doped SrO nanocomposites; molecular docking analysis, *J. Photochem. Photobiol., A*, 2023, **444**, 114970.